RSC Advances

PAPER

View Article Online
View Journal | View Issue

Cite this: *RSC Adv.*, 2024, **14**, 19528

Structural features of biobased composite foams revealed by X-ray tomography†

Swapnil Morankar, ‡[a] Rebecca Mort,‡[bc] Greg Curtzwiler, [cd] Keith Vorst,[cd] Shan Jiang *[bc] and Nikhilesh Chawla*[a]

Polymer foams can have heterogeneous and complex internal structures, especially when material blends or particles have been integrated to create composites. It becomes even more challenging to probe and understand foam structure/properties when using non-uniform particles, such as biobased fillers. Optical or SEM imaging can only provide limited information as these are two-dimensional (2D) surface techniques. In this study, 3D X-ray tomography was applied to comprehensively analyze the structural features of biobased polyurethane foams containing porous rice hull fillers. The in-depth characterization at a wide range of length scale enabled us to quantify and obtain statistics of the unique trends in foam pore size and pore orientation corresponding to rice hull particle fraction and particle size. Rice hull particles were found to induce smaller cell formation. In addition, these biobased particles influenced cell expansion and caused cells to have less consistent orientation. Furthermore, after foam samples were subjected to cyclic compressive loading, X-ray tomography showed fractures in large (>100 μm) particles. This helps reveal the premature failing mechanism of composite foams with highly porous and coarse particles. The study elucidates novel microstructural evolution and deformation mechanisms using 3D X-ray tomography. The results offer new insights on internal structures for biobased composites and foams that are not previously possible through the conventional characterization tools.

Received 1st April 2024
Accepted 11th June 2024

DOI: 10.1039/d4ra02461c

rsc.li/rsc-advances

1. Introduction

Polymer foams are among the most common materials utilized in our daily life, from insulation, to lightweight packaging.[1,2] Recently, low-isocyanate polyurethane foams with improved stability and compression modulus have been successfully prepared from biosourced and landfill-diverted materials.[3] As researchers strive to develop more sustainable alternatives to traditional petroleum-based foams, the changes in materials and processes will inevitably lead to unique structural properties.[4–10] In order to understand the structure–property relationships in these materials, it is critical to reveal the complex microstructure of the foam.[11,12] Characterizing the internal foam structure comprehensively is a challenge. Traditional methods of foam imaging, such as scanning electron microscopy (SEM), are limiting, because viewing a sample from several angles requires multiple sample replicas with different cross-sections and the sample surface must be damaged by cutting or fracturing to reveal the cross-section. On the other hand, X-ray computed tomography (XCT) can provide a precise three-dimensional (3D) view of the internal microstructure non-destructively, thus eliminating concerns over defects in cut/fractured cross-sections.[13] Furthermore, XCT can provide fine resolution (~1 μm voxel size at the lab-scale micro XCT and ~50 nm in nano XCT) within big structures, which allows us to investigate the foam structures and identify the fine features of biobased fillers at the same time.

XCT has previously been used to study porous materials including polyurethane foams.[14–18] Singaravelu *et al.*[14] performed an *in situ* XCT analysis of expanded bead polyurethane foams to characterize a gradient cell structure with small cells close to interfaces and larger cells in the bulk. Many foam materials such as polymethacrylimide,[19] polystyrene,[20,21] polymer fiber composites,[22,23] and ceramic and metal foams[24–28] have been analyzed with similar XCT methods. X-ray computed tomography provides a robust way to non-destructively visualize the structure in three dimensions. The 3D datasets obtained using XCT can be further analyzed to quantify the structural parameters such as cell volume and ligament thickness, giving a complete and accurate view of the foam structure.

[a]*School of Materials Engineering, Purdue University, West Lafayette, IN 47907, USA. E-mail: nikc@purdue.edu*

[b]*Deparatment of Materials Science and Engineering, Iowa State University, Ames, IA 50011, USA. E-mail: sjiang1@iastate.edu*

[c]*Polymer and Food Protection Consortium, Iowa State University, Ames, IA 50011, USA*

[d]*Department of Food Science and Human Nutrition, Iowa State University, Ames, IA 50011, USA*

† Electronic supplementary information (ESI) available. See DOI: https://doi.org/10.1039/d4ra02461c

‡ Co-first authors.

In this work, micro XCT was used to examine composite castor oil and rice hull foams and reveal novel insights into internal structures and mechanical properties that could not have been possible through conventional microscopy analysis alone. Rice hulls were selected as a filler due to their widespread abundance,[29,30] low cost,[31] and primarily cellulosic composition.[32] Thus, by utilizing ground rice hulls, we have a means to divert biobased material from the landfill and control foam properties without chemical alterations. Foam samples were prepared with either coarse or fine rice hull particles where the particle size was controlled by grinding and sieving. Previous work has shown that after grinding, these particles generally have an anisotropic, flake-like morphology. The variation of particle size significantly influences the foam properties.[3] Furthermore, the addition of rice hull particles not only provides mechanical reinforcements but can also alter the cellular structure of these foams. For example, foam structures may be influenced by rice hull particles acting as nucleation sites for pores or by particles hindering the expansion of pores during the foaming process. In addition, the size and fraction of the rice hull particles could play a significant role in determining the evolution of structure and the mechanical performance of these foams.

To successfully predict and control the mechanical properties of these foams, it is important to understand how processing influences the evolution of the foam structure. To our knowledge, very few studies have been conducted on the detailed correlation between processing and structure–properties of biobased composite foams. In this work, we uncover the processing–structure–property relationships in bio-based composite foams using multiple experimental tools including X-ray computed tomography, scanning electron microscopy, compression testing, and cyclic creep-recovery testing. X-ray computed tomography enabled 3D visualization of the foam structure, while scanning electron microscopy provided a means to understand the structure at a smaller length scale, beyond the resolution limit of X-ray tomography. Furthermore, the 3D datasets obtained from X-ray tomography were utilized to statistically quantify the cellular structure of these composite foams. Using rigorous image analysis algorithms, we have accurately quantified the evolution of cell size and orientation as a function of varying nature of rice hull particle size and loading. The use of mechanical testing further enabled us to understand the impact of these structural parameters, such as cell size distribution and orientation, on mechanical properties. The analysis showed that the addition of rice hull particles led to an anisotropic cellular structure as well as anisotropic mechanical properties. Mechanical testing suggested that the particle morphology, including both particle anisotropy and internal porosity, caused a directional dependence of the compression modulus. The novelties of this work lie in the application of XCT to investigate complex composite foams with hierarchical porosity, and in elucidating the relationships among foam processing, structure, and properties. This approach has led to the discovery of unique foam failure mechanisms and direction-dependent properties, insights that were achievable only through the use of XCT.

2. Methods

2.1 Synthesis of foams

Polyurethane foam synthesis was carried out using the same procedure described elsewhere.[3] The method is briefly summarized here. Chemicals used include research grade castor oil, 4,4′-methylenediphenyl diisocyanate, and hexamethylene diisocyanate from Sigma-Aldrich (St. Louis, Mo). The catalyst was >95% purity dibutyltin dilaurate from TCI America (Portland, OR). The surfactant was VORASURF™ DC 2584 from Dow Chemical (Midland MI). The filler was rice hulls obtained from a commercial source while the blowing agent was deionized water. Filler particles were produced by grinding rice hulls in a cyclone mill and then sieving though a 350 μm mesh for coarse particles (CRH) and 150 μm mesh for fine particles (FRH). Rice hull particle morphology (size and shape) were thoroughly characterized in previous work.[3] CRH and FRH particles have an average size of 50 μm and 136 μm respectively. They are primarily cellulosic material with hydroxyl groups on the particles' surface available to react with isocyanates.[3] Foams were produced by first preparing a pre-polymer, reacting the pre-polymer with isocyanate and water, then allowing the foam to rise under ambient conditions. The pre-polymer is a mixture of castor oil, rice hull particles (if included), catalyst, surfactant, and a small portion of isocyanate. The control formulation did not contain any rice hull particles and had an isocyanate index of 0.75. Formulations containing rice hull particles were identical to the control with particles added as a weight fraction relative to the castor oil mass.

2.2 Scanning electron microscopy

Scanning electron microscopy (SEM) was used to image cross-sections of the foam samples. Sample cross-sections were prepared by using a razor blade to cut perpendicular to the foam rising direction. The samples were then sputter coated with iridium. Samples were imaged with a FEI Quanta-FEG 250 SEM operating at an accelerating voltage of 10 kV in variable pressure mode (30 Pa).

2.3 X-ray computed tomography

The structure of all the biofoams in the as-processed state was investigated using a commercial X-ray microscope (Zeiss Xradia Versa 620, Carl Zeiss, Dublin, CA). This microscope is equipped with an X-ray source having a tungsten target. The voltage for X-ray production can be varied from 30 kVp to 160 kVp, producing X-rays with maximum energies ranging from 30 keV to 160 keV. The maximum X-ray power obtainable at these energies varies from 2 W to 25 W, respectively. The X-rays are produced in a cone beam-shaped Bremsstrahlung radiation. Both the polymeric material and rice hull particles have low X-ray attenuation, resulting very little artifact in reconstruction.

Multiple scans with different resolutions were performed to visualize the cellular structure of these foams at multiple length scales. All scans were performed using a voltage of 40 kV and power of 3 W. 3201 projections in the range of 0° to 360° were acquired for all scans. The scout and zoom procedure was

implemented to perform scans at different resolutions. In this procedure, successive scans with increasing magnifications are performed, where the "scout" scan provides larger field of view but poorer resolution and allows the user to select the region of interest for higher resolution scan, referred to as "zoom" scan. Then, this zoom scan is used to select another region of interest to conduct the scan at even higher magnification, and so on. This first scan was carried out with a 0.4× objective and 1 s exposure time per projection and provided a uniform voxel size of 23.5 μm. The volume of interest was then identified using this scan to perform a zoom scan at higher resolution. The zoom scan was carried out using a 4× objective and a 3 s exposure time and provided a uniform voxel size of 3 μm. The same process was repeated to obtain another higher resolution scan that had a uniform voxel size of 0.7 μm. This scan was performed using a 20× objective and 15 s exposure time per projection. All scans were conducted using camera binning 2 with each projection containing 1024 × 1024 pixels. All scans were reconstructed using commercial Zeiss reconstruction software that is based on a filtered back-projection algorithm. The same scanning procedure was repeated for the characterization of post-fatigue samples. Following the scans, commercial image analysis software (Avizo 9.0, Thermo Fisher Scientific, Hillsboro, OR) was used for image analysis, visualization, and quantification of the microstructure.

2.4 Mechanical testing

One set of foam samples were fatigued through cyclic creep-recovery using a DMA 7e (PerkinElmer, Waltham, MA) with a parallel compression plate fixture. Testing was conducted under isothermal conditions at 25 °C. Samples were loaded into the instrument with the same orientation to ensure force was always applied parallel to the foam rising direction. Samples were held under a static force of 10 mN for 1 minute before cycling began. Each cycle consisted of a creep force applied for 1 minute followed by a recovery force (10 mN) applied for 2 minutes. Creep force was adjusted for each sample to achieve approximately 50 ± 5% strain. Each test consisted of 20 cycles.

Foam compression testing was carried out using the same procedure as previously published[3] only altering sample orientation. The tests were conducted with an Autograph AGS-J (Shimadzu Corp., Kyoto, Japan) universal electromechanical tester fitted with a 5 kN load cell. In previous work, samples were always oriented such that force was consistently applied parallel to the foam rising direction. In this work, the same formulations were tested with force applied perpendicular to the foam rising direction. Compressive modulus was calculated as the slope of the initial (<5% strain) linear portion of the stress–strain curve.

3. Results

Five castor oil foam formulations were prepared using the same methods as previously published.[3] The first formulation is a control containing no rice hull particles. The remaining four formulations contain 10 and 30 weight% of coarse rice hulls (CRH) and fine rice hulls (FRH). Correspondingly, the samples are hereon referenced with the names: control, 10CRH, 30CRH, 10FRH, and 30FRH. A thorough analysis of these foam structures was conducted with XCT. Fig. 1 showcases the resolution and scale of images acquired from XCT scans. In the XCT scans, particles can be distinguished from the polymer matrix due to both variation in density and the presence of micro-scale pores. Fig. 1a–c display the cellular structure of the control sample and Fig. 1d–f show representative images of rice hull-containing samples. For the control sample, XCT confirms the open cell structure initially viewed in SEM images (Fig. S1†). Additionally, rice hull particles were clearly seen fully encased within cell walls. The particles are typically anisotropic and flake-shaped with internal porosity heron referred to as micro-scale pores.

More importantly, with a 3D perspective, we can now determine that the cells are not spherical. The cells are ellipsoidal with the elongated axis parallel to the foam rising direction – a common occurrence in free-rise polyurethane foams.[33] Fig. 1a also shows that these foams have a few larger pores of 3–5 mm length (indicated by arrows) which are likely air bubbles introduced during mixing. Foam samples containing rice hull particles have a similar ellipsoidal open cell structure (see Fig. 1c and f). Quantitative differences in structural features between the control sample and samples with rice hulls will be discussed in detail later in this section.

The rice hull particles are scattered throughout the cell walls and struts. Many cell struts in Fig. 1d are noticeably thicker than the struts in Fig. 1b, likely due to the presence of the particles. Instances of particle clusters (see Fig. 1e) were observed. Multiple adjacent particles could be easily distinguished from one another by differences in orientation of micro-scale pores. Clear contrast between the particle and polymer matrix arises from differences in material density. However, the density of these particles is not homogenous, leading to some particles not having distinguishable boundaries separating them from the surrounding polymer.

The addition of rice hull particles can lead to a change in the size and orientation of foam cells, which could play a significant role in determining the mechanical behavior of these foams. To gain further quantitative insights into the structural changes caused by the addition of rice hull particles, the 3D datasets obtained from X-ray tomography were segmented and analyzed. Higher resolution scans with a uniform voxel size of 3 μm were used for quantification. As shown in Fig. 1, these foams contain an interconnected network of open cell pores, thus, separating individual cells becomes a difficult task. Identifying boundaries between adjacent cells is important to accurately get statistics on each individual cell. Manually separating adjacent cells is not a viable solution for such large datasets. The accurate separation and quantification of individual cells was achieved using an integrated image analysis approach that involved threshold segmentation followed by watershed analysis.[34] Greyscale thresholding separates foreground and background pixels based on a selected range of gray values.[35] The binarized datasets obtained after the threshold segmentation were analyzed using watershed analysis. The watershed algorithm uses a peaks and valleys approach to separate individual cells

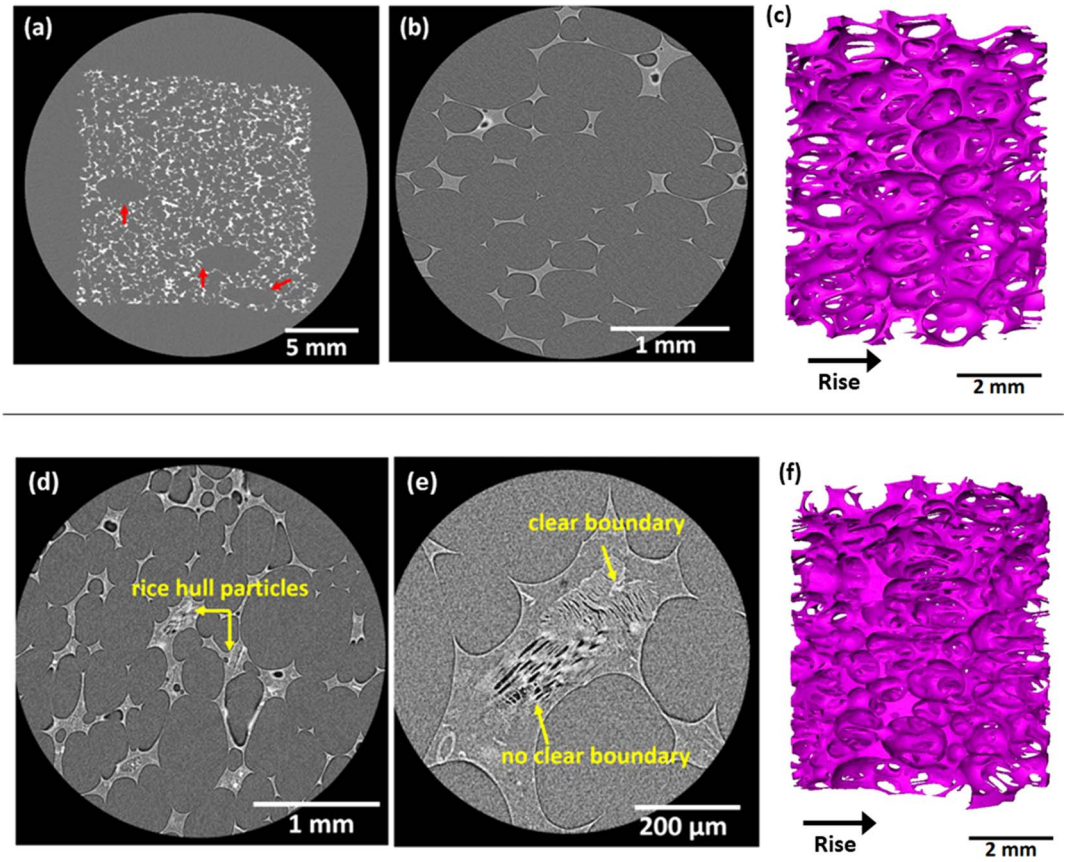

Fig. 1 Examples of foam structure particle cross-sections as seen on different scales (a) single scan of control sample with 0.4× objective, exposure time 1 second, and pixel size 23.5 μm, (b) single scan of control sample with 4× objective, exposure time 3 seconds, and pixel size 3 μm, (c) 3D rendering of control sample produced from a mid-level resolution scan (pixel size 3 μm) which has been segmented to show ligament structure, (d) mid-level resolution scan (pixel size 3 μm) showing several particles scattered throughout the structure, (e) high resolution scan (pixel size 0.7 μm) of two adjacent particles, (f) 3D rendering of 30FRH sample from a mid-level resolution scan (pixel size 3 μm). Particles are distinguished by the presence of "micro-scale pores" and, in some cases, a clearly discernible boundary arising from a difference in density between the particles and surrounding polymer matrix.

from the interconnected network.[36] More details about the image analysis protocol are given in the ESI (Fig. S2†). As shown in Fig. S2,† individual cells were accurately identified and separated using this integrated image analysis approach.

The 3D volume renderings of pores in each sample are shown in Fig. 2 and Table S1† lists data for the different parameters quantified for cells. The control sample (Fig. 2a) has cells which are consistent in packing, size, and orientation. The open cell structure causes 3D pores to be closely packed and in contact with one another. The 10FRH and 30FRH samples (Fig. 2b and c) show some notable differences. The pores in these samples appear smaller than those in the control sample. In addition to that, these samples contain several tiny pores which are not in contact with neighboring pores, indicating that these cells are closed rather than open. 30FRH has a noticeably higher number of smaller, closed cells than 10FRH. The samples with coarse rice hulls (Fig. 2d and e) also show a similar trend. The result of these structural changes is a more random distribution of cells, *i.e.*, more isotropic, with a significantly wider distribution in cell size.

Fig. 3a and b show histograms of cell volume. The quantification included approximately 100–200 cells in each sample. It appears that the cell volume distribution has shifted toward lower volume (left side) with the addition of rice hull particles. As discussed above, the addition of rice hull particles leads to the formation of smaller, closed cells. The insets of Fig. 3a and b show that these closed cells have a volume less than 5×10^6 μm^3. The control sample has 18% of cells with volume less than 5×10^6 μm^3. This number increased to 47% and 59% for the 10FRH and 30FRH samples and to 58% and 73% for the 10CRH and 30CRH samples, respectively. Fig. 3c shows the plot of average cell volume as a function of particle fractions. We can notice from Fig. 3c that the average cell volume also decreases as particle fraction increases. The decrease in cell volume is greater for CRH foams than for FRH foams. These results suggest that the biobased filler may act as a nucleation agent or trigger the formation of small cells by restricting cell expansion.

Cell orientation with respect to the foam rising direction was also measured (Fig. 3d and e). An orientation of 0° indicates the long axis of the cell is parallel to the rising direction. In the control sample, over 90% of cells are oriented with a small deviation (<10°). With the addition of rice hull particles, the distributions become broader and shift to the right, as the frequency of cells oriented >10° increases. The CRH and FRH

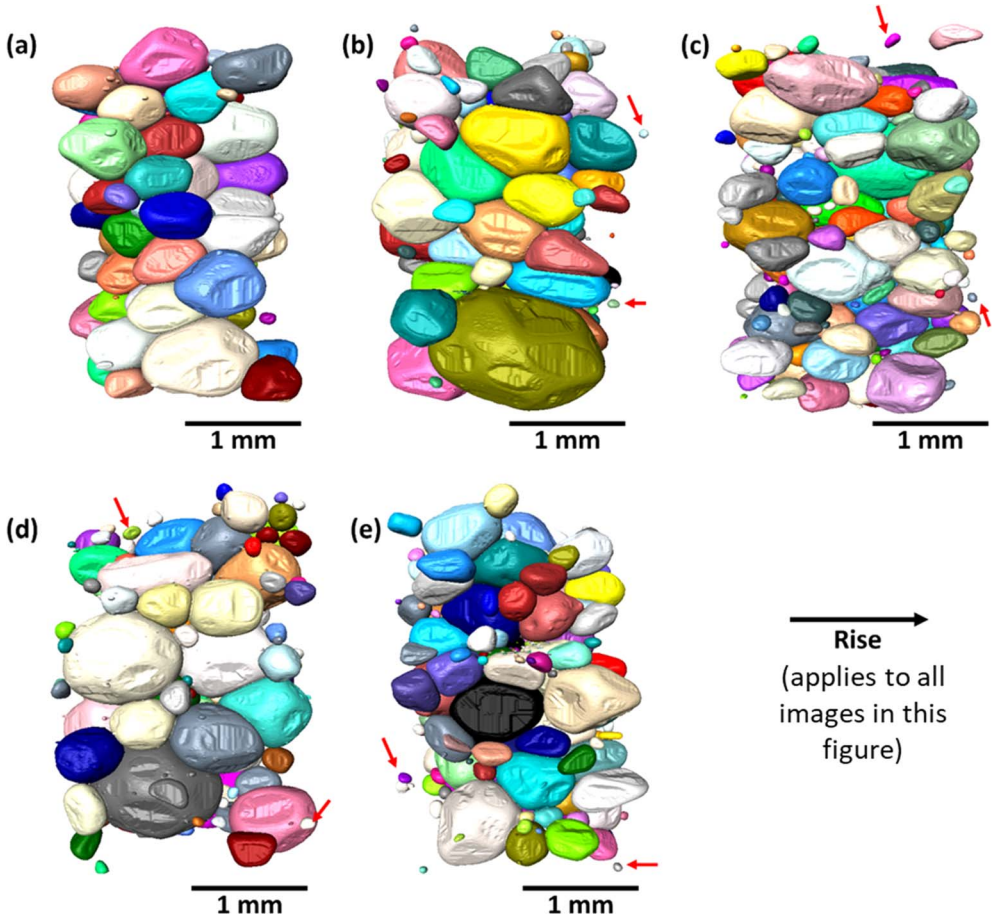

Fig. 2 3D renderings of separated pores within the foam structure generated from a mid-level resolution scan (pixel size 3 μm). (a) Control sample, (b) 10FRH, (c) 30FRH, (d) 10CRH, (e) 30CRH. The black arrow indicates the direction of rising and red arrows point to examples of small, closed pores.

foams have some instances of cells oriented 70–80°, nearly perpendicular to the rising direction. Fig. 3f shows the average orientation of cells with respect to rising direction. The average cell orientation for the 10FRH, 30FRH, 10CRH, and 30CRH are 13°, 17°, 21°, and 20° respectively. Therefore, coarse particles disrupt the alignment of cell orientation more than fine particles, though increasing the coarse particle fraction does not necessarily correspond to further disruption. Interestingly, the change in cell orientation does not correspond to a statistically significant change in cell aspect ratio. The aspect ratio in the control sample is approximately 1.5. As particle fraction increases, the aspect ratio remains consistent.

Given both the anisotropic nature of these foam structures and the influence rice hull particles have on cell orientation, it is reasonable to hypothesize that these foams may exhibit differences in mechanical properties depending on the direction of the property measurement. Previous work by Patterson *et al.* used *in situ* compression testing with XCT to demonstrate a correlation between foam structure and directional dependence of mechanical properties in polyurethane foams.[18] To test directional dependence, foam samples were compressed in two directions as shown in Fig. 4a and b. In the first scenario, compression force was applied parallel to the rising direction, and in the second scenario, force was applied perpendicular to the rising direction. Fig. S3† shows representative stress strain curves for each sample. The compression moduli, calculated as the slope of the stress strain curve in the initial linear region, were then compared (Fig. 4c). The percent change was calculated as parallel modulus divided by perpendicular modulus minus 100% (Fig. 4d). Thus, a positive% change implies the perpendicular modulus is higher and a negative% change implies the parallel modulus is higher. The control sample has a slightly lower parallel modulus (67 kPa) than perpendicular modulus (72 kPa). This is likely due to the foam structure anisotropy as pores are elongated in the parallel direction indicated by XCT scan. On the other hand, all particle-containing foams have higher parallel modulus than perpendicular modulus. This phenomenon is most significant in the coarse rice hull samples, where the percent change for 10CRH and 30CRH is −43% and −39% respectively. Given that the rice hull particles disrupt cell orientation, it is interesting that the rice hull containing samples display significantly more property inhomogeneity compared to the more aligned control sample. This suggests additional factors, such as particle morphology and particle alignment in cell walls are likely to have a greater influence over mechanical performance than cell alignment.

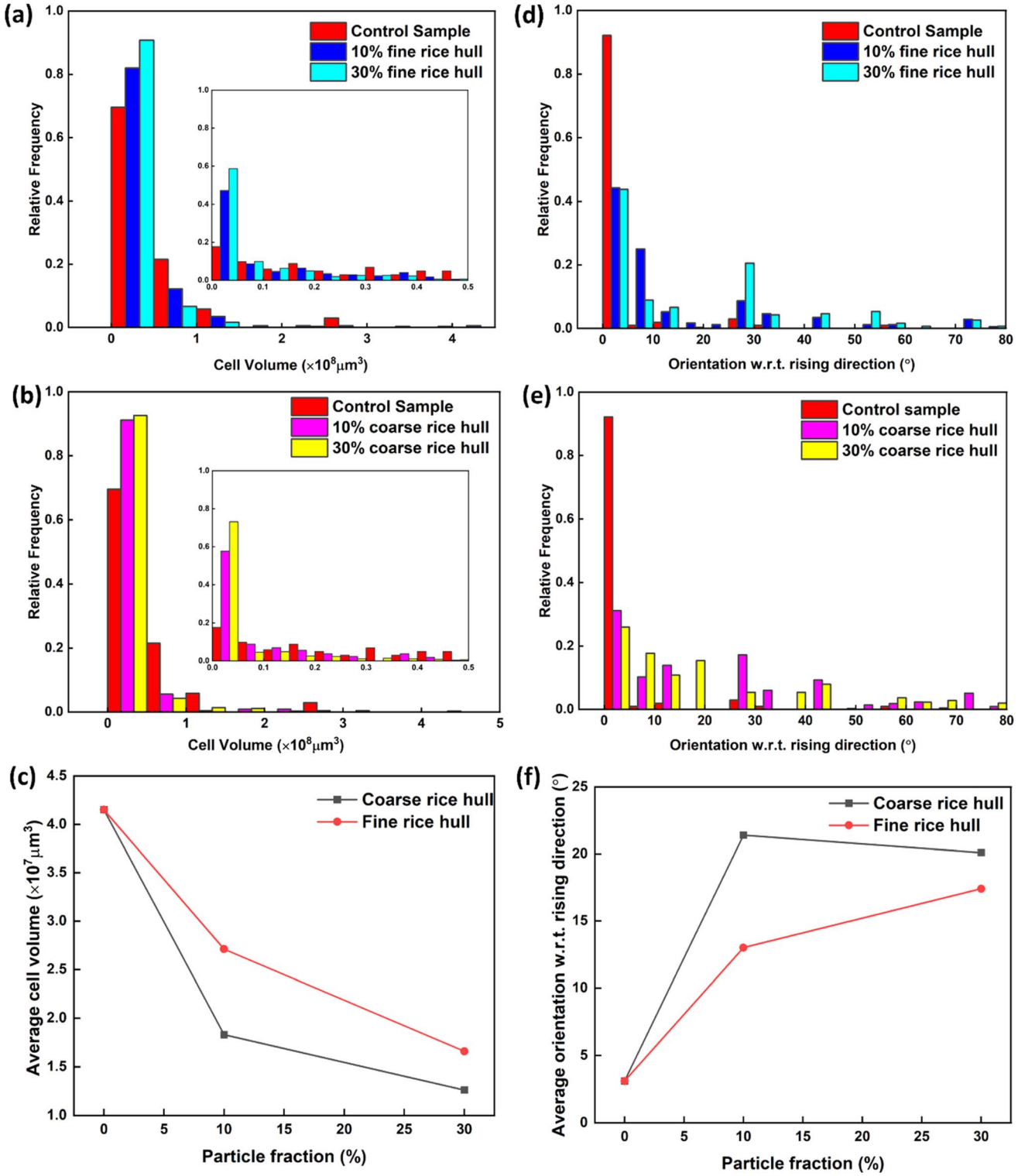

Fig. 3 Cell size and orientation data calculated from 3D segmented images. (a) FRH foam cell volume distribution, (b) CRH foam cell volume distribution, (c) change in average cell volume with increasing particle fraction, (d) FRH foam cell orientation distribution with respect to rising direction, (e) CRH foam cell orientation distribution, (f) change in average cell orientation with increasing particle fraction.

XCT also enabled observation of internal mechanical damage in these foams. Foam samples were mechanically fatigued through multiple creep-recovery cycles where the maximum strain was approximately 50%. Creep-recovery cycle data is provided in the ESI (Fig. S4).† Foams in cushioning and packaging applications will experience multiple stress loading cycles over the product lifetime and the ability to recover the original shape is an important indicator of durability over long

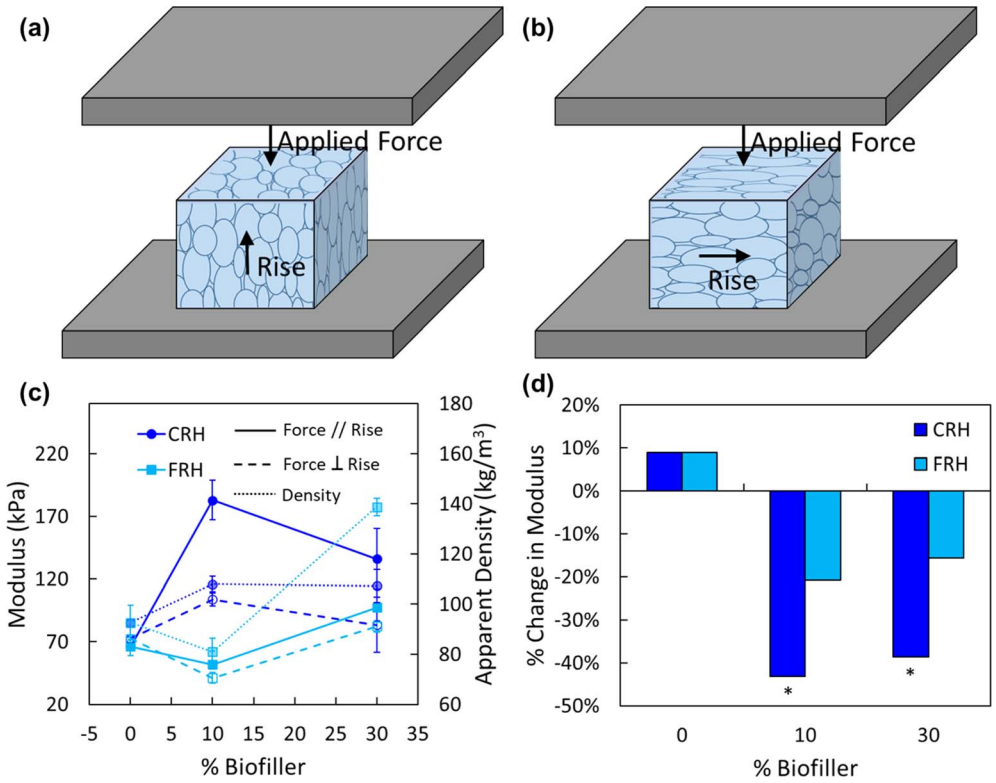

Fig. 4 Compression testing with changing orientation. Schematic of foam sample between compression platens with (a) force applied parallel (//) to rising direction, (b) force applied perpendicular (⊥) to rising direction. Compression testing data displayed in terms of (c) modulus *versus* particle fraction and apparent density data, (d) the change in modulus in parallel direction relative to perpendicular direction. Parallel modulus and density data shown in (c) was reported in the previous work by Mort *et al.*[3] Bars in (d) marked with * indicate the change is statistically significant within a 95% confidence interval using a one-way ANOVA with *post hoc t*-test.

term use. Fig. 5 shows representative examples of structural damage. The control sample (Fig. 5a) has multiple ligament fractures but does not show visible signs of permanent deformation. This observation is supported by the residual strain data reported in the original study, where the control sample had only 3.1% permanent strain following 20 creep-recovery cycles.[3] Samples containing particles also experienced ligament fracture (Fig. 5c–e). In addition, particles themselves experience internal fracture (Fig. 5b and d). If particle delamination (*i.e.*, adhesive failure) had occurred, we would see a clear gap between polymer matrix and in-tact particles. Instead, it appears the particles fractured along internal micro-scale pores (*i.e.* cohesive failure). The cohesive failure of particles could be partially responsible for the increased permanent strain seen in foams with rice hulls. Interestingly, there were no cases of particle fracture or delamination observed in particles with less than 100 μm Feret length (the largest distance between two parallel tangential lines in any in-plane direction of a flake). It is possible that these particles have a lower probability of having a strength-limiting flaw, or that they are simply more difficult to distinguish from the polymer matrix, making it consequently more difficult to identify instances of small particles exhibiting signs of damage. Small particles are also likely to form agglomerates, which would be more prone to mechanical damage due to the mechanical weaknesses at particle–particle interfaces. Single particles with amorphous (non-crystalline) regions would be far tougher and resist fracture. Additionally, several instances of apparently undamaged particles directly adjacent to fractured particles were observed.

4. Discussion

The results outlined in the previous section reveal several unique structural features and structure–property relationships in rice hull composite polyurethane foams. In the initial study, in depth characterization of mechanical and thermal properties was performed.[3] The key mechanical and thermal properties from the previous study are summarized in Table 1.

The data summarized in Table 1 shows that rice hulls generally increase foam density and compression modulus. Fig. 4c shows how density and compression modulus follow the same trend. This correlation was discussed in depth in previous work.[3] It is noteworthy that despite the general correlation, density alone cannot explain all mechanical property behavior. For instance, 10CRH and 30CRH have nearly identical densities, but significantly different compressive moduli. 30FRH has the highest density out of all samples, but still has a far lower compressive modulus compared to the CRH foams. Coarse particles can dramatically increase compression modulus by up to three-fold, but also cause a corresponding increase in compression modulus variability. Composite foams also have

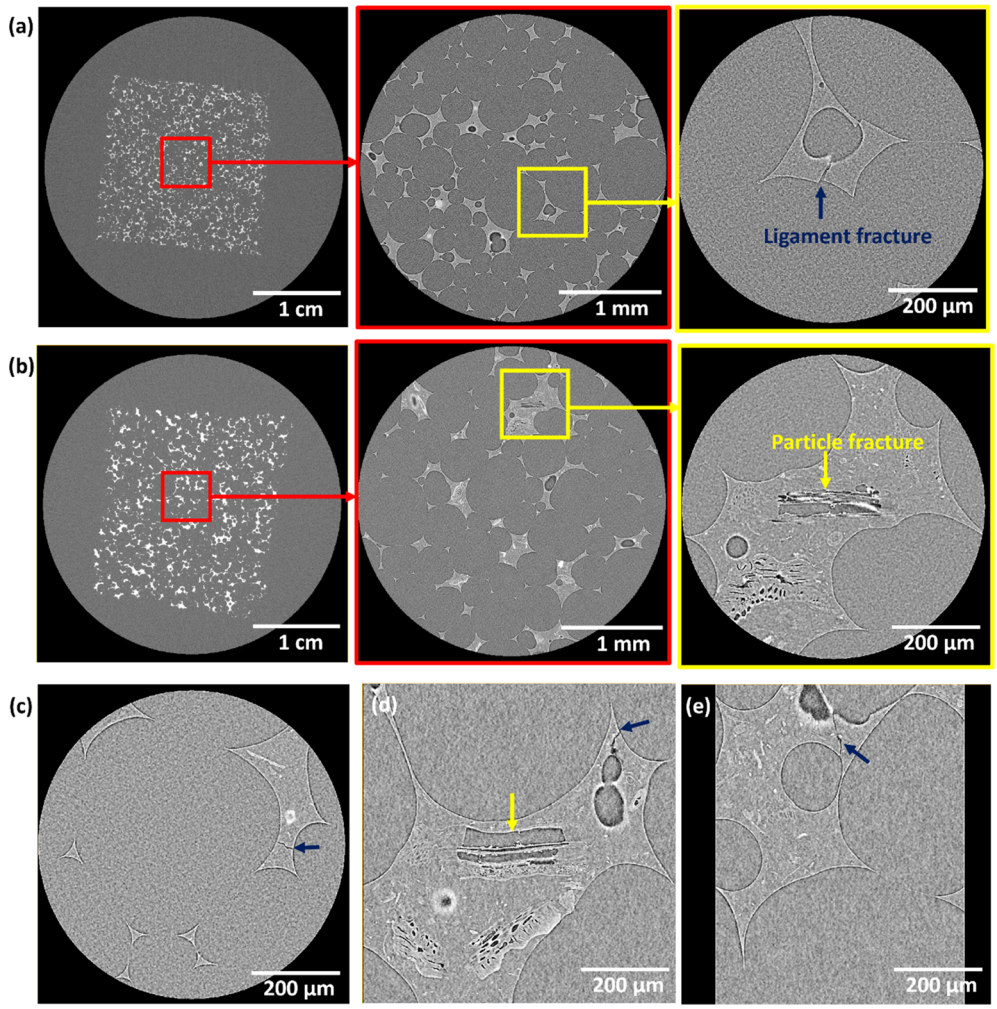

Fig. 5 Reconstructed 2D transverse slices of samples after undergoing 20 consecutive creep-recovery cycles. (a) Multiscale scan of control sample, (b) multiscale scan of 30FRH, (c)–(e) high resolution scans of 30FRH showing examples of damage from creep-recovery tested. Blue arrows indicate fractured ligaments and yellow arrows indicate damaged particles.

more permanent deformation after undergoing repeated applied stress compared to the control. XCT analysis provided the necessary 3D perspective and subsequent quantitative structural data to better understand (1) how rice hull particles influence foam structure, and (2) how the structural features correlate with mechanical properties.

XCT of the control sample (Fig. 1a–c) confirmed an open cell structure. The cells are ellipsoidal in shape, with the long axes oriented parallel to the foam rising direction. The XCT scans of samples containing particles (Fig. 1d and e) also show ellipsoidal open cells with particles fully embedded within cell struts. The particles, interestingly, have their own internal porosity. These micro-scale pores generally follow the same orientation as the individual particle. It should be noted that it was difficult to observe smaller particles (<50 μm) in either SEM or XCT. The lack of consistent contrast between particle and

Table 1 Foam formulation nomenclature and properties of foam formulations as reported in the previous study.[3] Compression modulus and creep-recovery test data shown were collected with samples oriented such that force was applied parallel to the foam rising direction

Sample name	Particle type	Particle weight%	Apparent density (kg m^{-3})	Compression modulus (kPa)	Stress at 50% strain (kPa)	Residual strain after 20 creep-recovery cycles (%)	Thermal conductivity (mW m^{-1} K^{-1})
Control	—	0	93 ± 7	66.6 ± 7.3	11.1 ± 1.9	3.1	46 ± 2
10CRH	Coarse rice hull	10	108 ± 2	182.6 ± 15.9	30.1 ± 2.2	23.3	47 ± 3
30CRH		30	107 ± 7	136.0 ± 23.9	31.9 ± 2.8	17.4	59 ± 5
10FRH	Fine rice hull	10	90 ± 5	51.7 ± 1.7	11.5 ± 2.1	20.2	47 ± 4
30FRH		30	139 ± 3	98.0 ± 3.0	36.7 ± 6.2	8.9	60 ± 2

polymer matrix means that distinguishing a particle's boundary is not always possible. The finer particles may also have fewer micro-scale pores, having been eliminated during the grinding process.

The overall foam cell structure has been quantified. Following the image analysis steps outlined by Fig. S2,† 2, and 3 it was possible to visualize individual cells and perform statistics on cell data sets. The 3D renderings presented in Fig. 2 revealed that the presence of rice hull particles disrupted the growth and organization of the cell structure. Both fine and coarse rice hull particles caused the formation of small, closed cells scattered throughout the otherwise open cell structure. This suggests large particles or particle agglomerates may be capable of restricting cell expansion. Furthermore, in 30CRH in particular, the overall average cell size appears to decrease significantly. As particle fraction increases, average cell volume decreases and fewer cells are strongly oriented (<10°) with the rising direction. These trends are also more drastic in CRH samples than in FRH samples. There are multiple ways in which rice hull particles could be affecting these structural properties.

Cell size in free-rise polyurethane foams is determined by several factors such as surfactant selection,[35] temperature,[36] and homogeneous *vs.* heterogeneous nucleation.[37] Previous studies have shown that using particles as heterogeneous nucleation sites results in a reduction of final cell size due to the higher number of bubbles initially formed.[37] Heterogeneous nucleation is a possible mechanism of the cell size trends observed in these rice hull composite foams, though more studies are needed to support this hypothesis. Another possible mechanism to explain cell size trends is rice hull particles impeding cell expansion by altering local viscosity and flow behavior. When particles are present in a high enough concentration to form aggregates,[38] it is feasible that such aggregates could significantly alter local flow patterns.[39] Very large and irregularly shaped particles may have a similar effect. This hypothesis could account for the presence of the small, closed cells which might have effectively been trapped by surrounding particle aggregates. It also provides an explanation for change in cell orientation (Fig. 3f). The ground CRH and FRH particles have apparent densities of 0.528, and 0.438 g cm^{-3} respectively.[3] The higher density and overall mass of very large particles and aggregates means that they might also be impacted by gravitational pull. Gravity could therefore act as an opposing force to the flow patterns during rising, causing the particles to get pulled downward and forcing cell orientation to shift. This would help explain why the coarse rice hull foams displayed far greater shifts in cell orientation than the fine rice hull foams.

The anisotropic structure of these foams has important implications for mechanical properties, such as compression modulus, which could change depending on the direction of the measurement. An experiment was conducted to test directional dependence by compressing samples either parallel or perpendicular to the rising direction (Fig. 4a and b). The cell orientation data collected from XCT shows the cells in the control sample are more oriented towards the rising direction than the samples with added rice hulls. This can help explain the ~9% difference between parallel and perpendicular moduli in the control sample, where perpendicular modulus is greater than parallel modulus. In contrast, both CRH and FRH foams had much higher differences (up to 43%), with parallel modulus consistently being higher than perpendicular modulus. These results suggest that the anisotropic particle morphology may play a bigger role than the cell orientation (Fig. 1e) within the composite foams. Previous work determined the number average aspect ratio of CRH and FRH particles were 0.7 and 0.6 respectively, where an aspect ratio less than 1 indicates elongation.[3] The thin flake-like shape of the particles should allow particles to follow the contour of the cell walls. Just as pores are stretched during foam rising, so is the material in the cell walls. Thus, it would be expected that particles are generally oriented with their longer axis aligned with the long axis of the cell. Therefore, it is likely that the added reinforcement in the parallel compression scenario arises from particle alignment.

The particles themselves still have their own internal microporosity, which will likely affect how the particle responds to stress applied in different directions. The orientation of pores will influence in which direction they are most likely to fail. Fig. 5d provides an example of neighboring particles which have differing responses to applied mechanical force. Only one particle experiences cohesive failure while the others do not show any clear signs of failure. The discrepancy must be attributed to the differences in particle orientation, particle density, and micropore orientation. Therefore, it is reasonable to conclude that the particle orientation and morphology has greater influence over mechanical properties than the foam cell structure alone. This may also provide further explanation for the compression modulus trend seen in CRH foams, where 10CRH has higher modulus than 30CRH (Fig. 4c). The coarser particles are more likely to be irregularly shaped and form bigger aggregates than the finer particles,[3] and aggregation may cause more randomness in particle orientation. Not only would these aggregated particles have their long axes oriented with the contour of the cell, but there are also new interfaces to consider. In a cluster of particles, inter-particle interactions will be weaker than an individual particle, making agglomerates more susceptible to shear forces.

Finally, to better understand how stress affects foam structure, a set of samples were mechanically fatigued prior to XCT analysis. The creep-recovery data presented in Table 1 shows that the control sample has the least amount of permanent deformation (*i.e.*, the sample mostly recovered to its original shape). Fig. 5a supports these results as the only evidence of structural damage are sporadic ligament fractures. These ligament fractures do not hinder the polymer from returning to its original shape after force is removed. Addition of rice hull particles increases permanent deformation. Prior to XCT analysis, it was suspected the permanent strain could have arisen from particles which had delaminated from polymer matrix, creating a gap but otherwise leaving the polymer and particle intact. However, as seen in Fig. 5b and d, the images suggest that the primary mechanism for permanent deformation was particle cohesive failure rather than adhesive failure. Previous research by Mort *et al.*[3] showed that due to the presence of hydroxyl groups on the particles' surface, rice hulls were capable

of reacting with isocyanates. Therefore, it is possible for particles to be covalently bonded to the polyurethane matrix, which would result in strong adhesion at the particle–polymer interface. The reaction kinetics of the rice hull hydroxyl groups compared to the castor oil hydroxyl groups has not been directly studied. Thus, the percentage of reacted hydroxyl groups in the coarse and fine rice hulls is unknown. This unexpected and distinctive cohesive failure mechanism indicates that the limiting factors influencing permanent deformation are the properties of the particles themselves. Reducing particle size aids in eliminating potential crack propagation sites, but higher particle loading is needed to increase modulus.

Another interesting observation in Fig. 5d is that though one particle is fractured, adjacent particles of similar size are not. These adjacent particles may not have failed due in part to a difference in the orientation of micro-scale pores and/or difference in material density. This could give rise to the directional dependence of compression modulus as stated previously. Furthermore, clear particle damage of any kind was only observed in particles with >100 μm Feret length. It is possible smaller particles experience damage as well but limitations in contrast between particle and polymer made it challenging to observe. Another explanation is that smaller particles may have fewer points of mechanical weakness due to lower porosity. This would explain why CRH foams experience higher permanent deformation than FRH foams.

5. Conclusions

In this work, the unique structural features of composite castor oil–rice hull polyurethane foams were revealed through XCT. Quantitative characterization of foam structure not only allowed us to better understand how rice hull particles of different sizes affect foam formation, but also provided insight into structure–property relationships. Crucially, the mechanical performance of these composite foams is not only determined by the overall foam structure, but also by the morphology of the rice hull particles. XCT allowed us to visualize and quantify the 3-dimensional structure of these foams, revealing multiple unique features including the presence of abnormally small, closed cells within an otherwise open cell structure as well as the reduced orientation of the cells. The major learnings about the composite foam structure–property relationships in this study are as follows:

- Rice hull particles lead to smaller cells on average, including several small, closed cells.
- The flake-like particles align with the orientation of the cells such that the long particle axes provide greater reinforcement when force is applied parallel to the rising direction.
- Large particles and particle agglomerates are the driving forces in foam structure change, leading to smaller cells and less consistent cell organization in CRH foams compared to FRH foams.
- Cohesive failure of large particles leads to permanent deformation. Durability can be improved simply by reducing particle size.

Future work such as *in situ* synchrotron XCT could further improve knowledge of bubble nucleation during synthesis and real-time mechanical response to compression. Furthermore, particle selection could be expanded to other biobased agricultural waste materials such as coffee chaff, corn stover, or wheat straw. By introducing different particle morphologies, a more complete theory of particle influence over foam properties and failure mechanisms can be developed. Ultimately, understanding the mechanisms which determine foam structural properties will enable ways to produce more effective and sustainable composites in the future.

Ethical statement

No experiment involving human tissue was carried out.

Data availability

The data processing code and a DOI to an electronic repository can be provided upon request.

Conflicts of interest

Keith Vorst and Greg Curtzwiler are listed as inventors under a patent related to this research. The patent is owned by Iowa State University.

Acknowledgements

This work was supported in part by the Polymer and Food Protection Consortium (PFPC) at Iowa State University under grant number GR-025895-00001 DD11523 and the Agricultural and Home Economics Station (HATCH Project 04202). Dr Shan Jiang and Rebeca Mort would also like to acknowledge Biobased Products Funding support from Iowa State University under grant number GR-026097-00001.

References

1 M. Ates, *et al.*, Polyurethane foam materials and their industrial applications, *Polym. Int.*, 2022, **71**(10), 1153–1252.
2 R. Hasanzadeh, *et al.*, A review of the state-of-the-art on thermal insulation performance of polymeric foams, *Therm. Sci. Eng. Prog.*, 2023, **41**, 101808.
3 R. Mort, *et al.*, Low-isocyanate polyurethane foams with improved stability and compression modulus prepared from bio-sourced and landfill-diverted materials, *ACS Appl. Polym. Mater.*, 2023, **5**(9), 7602–7613.
4 R. Mort, *et al.*, Biofillers improved compression modulus of extruded PLA foams, *Sustainability*, 2022, **14**(9), 5521.
5 B. Wicklein, *et al.*, Thermally insulating and fire-retardant lightweight anisotropic foams based on nanocellulose and graphene oxide, *Nat. Nanotechnol.*, 2015, **10**(3), 277–283.
6 G. Wang, *et al.*, Ultralow-threshold and lightweight biodegradable porous PLA/MWCNT with segregated conductive networks for high-performance thermal insulation and electromagnetic interference shielding

applications, *ACS Appl. Mater. Interfaces*, 2018, **10**(1), 1195–1203.
7 J. Wang, *et al.*, Strong and thermally insulating polylactic acid/glass fiber composite foam fabricated by supercritical carbon dioxide foaming, *Int. J. Biol. Macromol.*, 2019, **138**, 144–155.
8 Z. Qu, *et al.*, Cellular morphology evolution in nanocellular poly (lactic acid)/thermoplastic polyurethane blending foams in the presence of supercritical N_2, *Eur. Polym. J.*, 2019, **116**, 291–301.
9 Y. Chen, *et al.*, Dual-Enhanced Hydrophobic and Mechanical Properties of Long-Range 3D Anisotropic Binary-Composite Nanocellulose Foams *via* Bidirectional Gradient Freezing, *ACS Sustainable Chem. Eng.*, 2019, **7**(15), 12878–12886.
10 J. Zhang, N. Hori and A. Takemura, Reinforcement of agricultural wastes liquified polyols based polyurethane foams by agricultural wastes particles, *J. Appl. Polym. Sci.*, 2021, **138**, 50583.
11 R. Mort, *et al.*, Biobased foams for thermal insulation: material selection, processing, modelling, and performance, *RSC Adv.*, 2021, **11**, 4375–4394.
12 Y. Pang, *et al.*, A comprehensive review of cell structure variation and general rules for polymer microcellular foams, *Chem. Eng. J.*, 2022, **430**, 132662.
13 P. J. Withers, *et al.*, X-ray computed tomography, *Nat. Rev. Methods Primers*, 2021, **1**, 18.
14 A. S. S. Singaravelu, *et al.*, Poisson's ratio of eTPU molded bead foams in compression *via in situ* synchrotron X-ray microtomography, *J. Mater. Sci.*, 2021, **56**, 12920–12935.
15 A. S. S. Singaravelu, *et al.*, In situ X-ray microtomography of the compression behavior of eTPU foams with a unique graded structure, *J. Mater. Sci.*, 2021, **56**, 5082–5099.
16 D. S. Bolintineanu, *et al.*, Anisotropy evolution of elastomeric foams during uniaxial compression measured *via* in-situ X-ray computed tomography, *Materialia*, 2021, **18**, 101112.
17 A. Nistor, *et al.*, Tomographic reconstruction and morphological analysis of rigid polyurethane foams, *Macromol. Symp.*, 2016, **360**(1), 87–95.
18 B. M. Patterson, *et al.*, Morphological and Performance Measures of Polyurethane Foams Using X-Ray CT and Mechanical Testing, *Microsc. Microanal.*, 2014, **20**(4), 1284–1293.
19 H. W. Chai, *et al.*, Microstructural characterization and constitutive modeling of deformation of closed-cell foams based on *in situ* x-ray tomography, *Int. J. Plast.*, 2020, **131**, 102730.
20 R. Meftah, *et al.*, X-ray Computed Tomography for Characterization of Expanded Polystyrene (EPS) Foam, *Materials*, 2019, **12**(12), 1944.
21 L. Andena, *et al.*, Compression of polystyrene and polypropylene foams for energy absorption applications: A combined mechanical and microstructural study, *J. Cell. Plast.*, 2018, **55**(1), 49–72.
22 E. Dilonardo, *et al.*, High resolution X-ray computed tomography: A versatile non-destructive tool to characterize CFRP-based aircraft composite elements, *Compos. Sci. Technol.*, 2020, **192**, 108093.
23 H. Shen, S. Nutt and D. Hull, Direct observation and measurement of fiber architecture in short fiber-polymer composite foam through micro-CT imaging, *Compos. Sci. Technol.*, 2004, **64**(13–14), 2113–2120.
24 Y. Ni, *et al.*, Investigations of the failure behaviors of open-cell copper foam based on in-situ X-ray tomography compression experiments and image reconstructed finite element modeling, *Eng. Fract. Mech.*, 2022, **263**, 108323.
25 M. A. Kader, *et al.*, Geometrical and topological evolution of a closed-cell aluminum foam subject to drop-weight impact: An X-ray tomography study, *Int. J. Impact Eng.*, 2020, **139**, 103510.
26 X. Ou, *et al.*, X-ray micro computed tomography characterization of cellular SiC foams for their applications in chemical engineering, *Mater. Charact.*, 2017, **123**, 20–28.
27 E. Gregorova, *et al.*, Microstructure characterization of mullite foam by image analysis, mercury porosimetry and X-ray computed microtomography, *Ceram. Int.*, 2018, **44**(11), 12315–12328.
28 C. Petit, *et al.*, Two-scale study of the fracture of an aluminum foam by X-ray tomography and finite element modeling, *Mater. Des.*, 2017, **120**, 117–127.
29 K. C. Onyelowe, *et al.*, Morphology and minerology of rice husk ash treated soil for green and sustainable landfill liner construction, *Cleaner Mater.*, 2021, **1**, 100007.
30 Service, U.E.R, Rice Sector at a Glance, 2022, June 2023, available from: **https://www.ers.usda.gov/topics/crops/rice/rice-sector-at-a-glance/#**.
31 USDA, *Weekly National Rice Summary Mon Oct 24, 2022*, USDA AMS Livestock, Poultry and Grain Market News, Little Rock, AR, 2022.
32 L. K. Lazzari, *et al.*, Production of carbon foams from rice husk, *Mater. Res.*, 2019, **22**, 0427.
33 L. J. Gibson and M. F. Ashby, Cambridge Solid State Science Series, *Cellular Solids*, Cambridge University Press, Cambridge, 2nd edn, 1997.
34 J. Zhang, *et al.*, The development of a 3D mesoscopic model of metallic foam based on an improved watershed algorithm, *Modell. Simul. Mater. Sci. Eng.*, 2018, **26**, 045008.
35 S. M. Hasan, *et al.*, Development of siloxane-based amphiphiles as cell stabilizers for porous shape memory polymer systems, *J. Colloid Interface Sci.*, 2016, **478**, 334–343.
36 J. Wang, *et al.*, A review of research on the effect of temperature on the properties of polyurethane foams, *Polymers*, 2022, **14**(21), 4586.
37 S. Perez-Tamarit, *et al.*, In-situ understanding of pore-nucleation and growth in polyurethane foams by using real-time synchrotron X-ray tomography, *Polymer*, 2019, **166**, 50–54.
38 C. F. Mora, A. K. H. Kwan and H. C. Chan, Particle size distribution analysis of coarse aggregate using digital image processing, *Cem. Concr. Res.*, 1998, **28**(6), 921–932.
39 M. M. Rueda, *et al.*, Rheology and applications of highly filled polymers: a review of current understanding, *Prog. Polym. Sci.*, 2017, **66**, 22–53.